



## Supported N-doped carbon quantum dots as the highly effective peroxydisulfate catalysts for bisphenol F degradation

Jifei Hou<sup>a</sup>, Hong Li<sup>a</sup>, Yuqiong Tang<sup>a</sup>, Jingya Sun<sup>a</sup>, Heyun Fu<sup>a,\*</sup>, Xiaolei Qu<sup>a</sup>, Zhaoyi Xu<sup>a</sup>, Daqiang Yin<sup>b</sup>, Shourong Zheng<sup>a,\*</sup>

<sup>a</sup> State Key Laboratory of Pollution Control and Resource Reuse, Jiangsu Key Laboratory of Vehicle Emissions Control, School of the Environment, Nanjing University, Nanjing 210093, PR China

<sup>b</sup> Key Laboratory of Yangtze River Water Environment of Ministry of Education, Tongji University, Shanghai 200092, PR China



### ARTICLE INFO

#### Keywords:

Bisphenol F degradation  
Catalytic peroxydisulfate activation  
Advanced oxidation processes  
Supported N-doped carbon quantum dots  
Support effects

### ABSTRACT

As an alternative additive for bisphenol A, bisphenol F (BPF) also has very strong endocrine-disrupting effects. In the present study, N-doped carbon quantum dots (NCQDs) supported on three supports (e.g., SiO<sub>2</sub>, ceria-zirconia solid solution/CeZrO<sub>2</sub> and γ-Al<sub>2</sub>O<sub>3</sub>) were prepared, and catalytic peroxydisulfate (PDS) activation for BPF degradation was investigated. Catalyst characterization results showed that NCQDs were highly dispersed on the surface of both Al<sub>2</sub>O<sub>3</sub> and CeZrO<sub>2</sub> due to strong electrostatic attractive interactions between NCQDs and supports, while remarked agglomeration of NCQDs was identified on SiO<sub>2</sub> surface because of repulsive interactions between NCQDs and SiO<sub>2</sub> support. For the catalytic PDS activation for BPF degradation, the catalysts displayed an increasing catalytic activity ordered as: NCQD/SiO<sub>2</sub> < NCQD/CeZrO<sub>2</sub> < NCQD/Al<sub>2</sub>O<sub>3</sub>. The higher catalytic activity of NCQD/Al<sub>2</sub>O<sub>3</sub> was ascribed to its higher NCQDs dispersion and stronger adsorption of PDS on the catalyst. Accordingly, the reaction of adsorbed PDS and BPF was found to be the rate controlling steps, which could be well described using the binary Langmuir-Hinshelwood model. Moreover, a volcano type dependence of BPF degradation rate on the NCQDs loading amount over Al<sub>2</sub>O<sub>3</sub> was identified. The degradation intermediates of BPF were identified using gas chromatography-mass spectrometer and the degradation pathway was proposed. The present findings highlight that NCQDs supported on Al<sub>2</sub>O<sub>3</sub> can be used a highly active catalyst in PDS activation for the degradation of organic pollutants.

### 1. Introduction

As an alternative additive for bisphenol A (4,4'-isopropylidenediphenol, BPA), bisphenol F (4,4'-dihydroxyphenol-methane, BPF) is an important monomer raw material, which has been widely used in resin and plastic industry without specific environmental discharge regulation [1]. In accordance, BPF has been frequently identified in daily necessities (e.g., personal care products, paper products and food) [2], indoor dust [3], surface water, and sediment [4,5]. However, toxicity studies indicated that similar to BPA, BPF exhibited very strong estrogenic and antiandrogenic effects in vivo or vitro experiments [6–9]. Additionally, the estrogenic activity of BPF was found to be even 5 times higher than that of BPA based on the result of human MCF-7 cell proliferation test [10,11]. Moreover, BPF may form higher toxic aromatic halogenated disinfection byproducts, during drinking water treatment processes [12–14]. Considering its very strong endocrine-disrupting effects on human, it is necessary to develop effective

methods to eliminate BPF in water.

Conventional treatment techniques, e.g., adsorption [15], chemical degradation [16] and biological treatment [17], have been used for the removal of endocrine disrupting chemicals. As highly effective chemical treatment methods, advanced oxidation processes (AOPs) have received wide attention in the abatement of endocrine disrupting chemicals [18–20]. Notably, sulfate radicals-based AOPs (SR-AOPs) have attracted increasing interests in water treatment due to the relatively high stability, broad applicable pH range and high redox potential of sulfate radicals, by which the endocrine disrupting chemicals could be completely mineralized into CO<sub>2</sub> and H<sub>2</sub>O. For SR-AOPs, persulfates (e.g., peroxydisulfate/PDS and peroxymonosulfate/PMS) could be activated by many methods, including physical (e.g., UV, heat, microwave, ultrasound) [21–24] and chemical methods (e.g., catalyzed by metal oxides and carbonaceous materials) [25–28]. Among these methods, catalysis using carbonaceous materials is regarded as the promising and green one in persulfate activation, due to the high catalytic activity and

\* Corresponding authors.

E-mail addresses: [heyunfu@nju.edu.cn](mailto:heyunfu@nju.edu.cn) (H. Fu), [srzhang@nju.edu.cn](mailto:srzhang@nju.edu.cn) (S. Zheng).

stability under a wide pH range without secondary pollution [26–40]. For example, Indrawirawan et al. [26] studied nanocarbons with different structural dimensions (0-3D) for PMS activation, and concluded that carbonaceous catalysts with graphitic carbon structure, high defective edge sites and low oxygen content possessed higher catalytic activity. Alternatively, Sun et al. [29] demonstrated that heteroatom nitrogen-doped carbon nanotubes had high catalytic activity. Notably, carbonaceous catalysts previously used for persulfate activation were commonly bulky ones with a low content of defect sites, which usually acted as catalytic active sites [29,32,33]. Considering that nitrogen-doped carbon quantum dots (NCQDs) had N-containing functionalities as well as a large amount of surface defects, we speculated that effective dispersion of NCQDs on support surface could result in highly active catalysts for persulfate activation. To the best of our knowledge, similar catalysts have not been reported for persulfate activation thus far.

In the present study, we prepared supported NCQDs catalysts on  $\text{SiO}_2$ , ceria-zirconia solid solution ( $\text{CeZrO}_2$ ) and  $\gamma\text{-Al}_2\text{O}_3$  and investigated PDS (a common persulfate) activation on the catalysts for BPF degradation. We selected  $\text{SiO}_2$ ,  $\text{CeZrO}_2$  and  $\gamma\text{-Al}_2\text{O}_3$  as the catalyst supports because of their high stability against thermal treatment at high temperature. Moreover, these supports have very different isoelectric points (IEPs) (i.e., 2.4 for  $\text{SiO}_2$ , 6.2 for  $\text{CeZrO}_2$  and 8.1 for  $\text{Al}_2\text{O}_3$ ), likely resulting in varied interactions with NCQDs and PDS. Additionally, the activation mechanism of PDS on the supported NCQDs was detected via electron paramagnetic resonance (EPR) spectroscopy. The intermediates of degraded BPF were detected via gas chromatography-mass spectrometry (GC-MS), and the degradation pathway of BPF was also proposed.

## 2. Experimental

### 2.1. Preparation of catalyst supports

We selected three supports to prepare supported catalysts, i.e.,  $\text{SiO}_2$ ,  $\text{CeZrO}_2$  and  $\gamma\text{-Al}_2\text{O}_3$ .  $\gamma\text{-Al}_2\text{O}_3$  was purchased from Shanghai Chem. Co., China.  $\text{SiO}_2$  was prepared using tetraethyl orthosilicate (TEOS) as the precursor. Typically, water, ethanol and ammonia ( $\text{NH}_3\text{H}_2\text{O}$ , 25 wt.%) were mixed with a molar composition of 8:5:0.4. Then, 30 mL of TEOS was added dropwise. After stirring for 5 h, the resulting white precipitant was filtered, washed with deionized water until neutral pH, and dried at 80 °C for 12 h.  $\text{CeZrO}_2$  (Ce/Zr molar ratio of 1:1) was prepared by the co-precipitation method. Briefly, 150 mL of 0.1 M  $\text{Ce}(\text{NO}_3)_3\text{6H}_2\text{O}$  and 150 mL of 0.1 M  $\text{ZrOCl}_2\text{8H}_2\text{O}$  were mixed under stirring, to which 0.2 M NaOH was added slowly until pH reached 10. After stirring for another 2 h at room temperature, the resulting solid was recovered by filtration, washing with deionized water until neutral pH, and drying at 80 °C for 12 h. Prior to the preparation of supported catalysts, the supports (i.e.,  $\text{SiO}_2$ ,  $\text{CeZrO}_2$  and  $\gamma\text{-Al}_2\text{O}_3$ ) were calcined in air at 750 °C for 2 h in a muffle furnace.

### 2.2. Preparation of NCQDs

NCQDs were obtained by a hydrothermal method using fumaronitrile as the precursors [41]. Typically, 0.6 g of fumaronitrile ( $\text{C}_4\text{H}_2\text{N}_2$ , > 98%, J&K Scientific Ltd., China) was added to 20 mL of deionized water, and the mixture was transferred into a 50 mL of self-pressurized autoclave with polytetrafluoroethylene lining, which was heated in an oven at 225 °C for 10 min. After cooling to room temperature, the resulting brown NCQDs solution was obtained by removing large particles by filtration using 0.22  $\mu\text{m}$  filtration membrane and was preserved in dark.

### 2.3. Preparation of supported NCQDs catalysts

Supported catalysts were prepared by the impregnation method. For  $\text{Al}_2\text{O}_3$  supported catalysts, 1.0 g of  $\text{Al}_2\text{O}_3$  was impregnated by a desired

amount of NCQDs solution (2–9 mL), and dried at 80 °C for 5 h. Then, supported NCQDs were loaded in an alumina ark, which were further carbonized at a preset temperature (500, 600, or 700 °C) for 1 h in a horizontal tube furnace under nitrogen atmosphere with a  $\text{N}_2$  flow rate of 50  $\text{mL min}^{-1}$ . The resulting supported catalyst was labeled as NCQD (x)/ $\text{Al}_2\text{O}_3$ -y, where x presents the loading amount of NCQDs (%), obtained from TG analysis, and y presents the carbonization temperature (°C). Similarly, NCQD(2.49)/ $\text{SiO}_2$ -700 and NCQD(1.77)/ $\text{CeZrO}_2$ -700 were also prepared using  $\text{SiO}_2$  and  $\text{CeZrO}_2$  as the supports. For comparison, unsupported NCQDs (i.e., powder NCQD/p-NCQD) were also prepared. It was obtained by drying NCQDs solution at 80 °C for 5 h and grinding to powder. Then, p-NCQD was further carbonized in nitrogen atmosphere at preset temperatures (500, 600, and 700 °C) for 1 h. The resulting black powder was labeled as p-NCQD-y, where y presents the carbonization temperature (°C). Some commercial carbons (graphite, activated carbon, and multi-walled carbon nanotubes/MW-CNTs) were investigated for comparison. Detailed information of these materials are listed in Table S1 in supporting information (SI).

### 2.4. Characterization of the catalysts

A Rigaku D/max-RA powder diffraction-meter equipped with  $\text{Cu K}\alpha$  ( $\lambda = 0.154 \text{ nm}$ ) radiation was used to give the X-ray diffraction (XRD) patterns of the catalysts. The specific surface area ( $S_{\text{BET}}$ ) of catalysts was detected on an ASAP 2020 instrument (Micromeritics Instrument Co., Norcross, GA, USA) at –196 °C (77 K), and was calculated by the Brunauer-Emmett-Teller (BET) method. The element content in the surface of the catalysts was determined by X-ray photoelectron spectroscopy (XPS) using an ESCALAB250Xi (Thermo Scientific, USA) with a monochromatized  $\text{Al K}\alpha$  excitation source ( $h\nu = 1486.6 \text{ eV}$ ). The binding energy values were calibrated by the C1s peak at 284.6 eV. The element compositions of the catalysts were determined on a Vario Micro cube elemental analyzer (Elementar Co., Germany). The TG-DTA curves were determined on an SII EXSTAR TGA/DTA 6300 thermogravimetric analyzer (Seiko Instruments Inc., Japan) with an air flow of 110  $\text{mL min}^{-1}$ . The transmission electron microscopy (TEM) images and the high angle annular dark field scanning transmission electron microscopy (HAADF-STEM) images were collected on an FEI Tecnai F20. Atomic force microscopy (AFM) images were used to characterize the height of NCQDs and were collected on a Multi Mode v8 scanning probe microscope (MM-SPM, Bruker, German) with a Scan Asyst Mode.

The isoelectric points (IEPs) of the supports and catalysts were determined on Nano ZS potentiometer (Malvern, UK). Briefly, the catalyst was added to deionized water containing 1  $\text{mmol L}^{-1}$  NaCl, obtaining a suspension concentration of 100  $\text{mg L}^{-1}$ . The suspension was sonicated for 30 min, and then stirred for 5 h to sufficiently disperse the catalyst particles. The suspension was evenly divided into nine parts to adjust the pH from 2 to 10 with 0.1  $\text{mmol L}^{-1}$  HCl or NaOH followed by standing for 24 h to stabilize pH. The surface zeta potentials of sample were detected via a potentiometer equipped with disposable folded capillary cells.

### 2.5. Catalytic degradation of BPF

The catalytic activities of supported NCQDs catalysts were evaluated by liquid phase catalytic degradation of BPF, which were conducted in a 250 mL of three-necked flask at room temperature. Briefly, 50 mg of catalyst was dispersed in 200 mL of 0.1 mM BPF aqueous solution under stirring for 1 h to reach adsorption equilibrium. The reaction was then started upon the addition of PDS. During the reaction, 1 mL of the reaction solution was taken at preset time, which was filtered using a 0.45  $\mu\text{m}$  filter and collected in a vial containing 0.5 mL of methanol as the free radical inhibitor. The residual BPF in the filtrate was analyzed on high performance liquid chromatography (HPLC, Agilent 1200 Series, USA) with an Eclipse XDB-C18 column (4.6 × 150 mm, 5  $\mu\text{m}$ ) and a UV detection wavelength of 230 nm.

Water-methanol solution (v/v, 35:65) was used as an isocratic eluent with a flow of 1.0 mL min<sup>-1</sup> for BPF analysis. The reaction conditions, such as catalyst dosage and initial BPF concentration, were carefully selected to avoid potential mass transfer limitations. Preliminary experiments showed that mass transfer limitations were absent under our experimental conditions (see Fig. S1 in SI).

EPR spectra were conducted on a Bruker EMX-10/12 spectrometer (Bruker, Bremen, Germany) to detect the active species generated in the activation of PDS. EPR was operated at centerfield of 348.2 mT, sweep width of 20 mT, microwave frequency of 9.77 GHz; modulation frequency of 100 kHz, and power of 20 mW.

The degradation intermediates of BPF produced via PDS oxidation were silanized and detected using GC–MS (Thermo Fisher Scientific, USA) equipped with a TR-5MS column. The details of operation were described as follows. Sample aliquot (2.5 mL) of the reaction solution was taken at preset time and added into a vial equipped with 5.0 mL dichloromethane (DCM) as extractant, which was shaken vigorously in a vortex mixture for 1 min. The mixture was allowed to stand for 2 h to separate water and DCM. Then, 0.5 mL of extract was transferred into a chromatographic vial and dried by nitrogen purging. Finally, the extract was silanized with 50 µL of N,O-bis(trimethylsilyl)trifluoroacetamide] containing 1% trimethylsilyl chloride (BSTFA + TMCS, 99:1) as the derivatization agent at 70 °C for 15 min under sealed conditions. Then, the derivatives were analyzed using GC–MS. The conditions for GC–MS analysis were set as follows: carrier gas was helium with a flow rate of 1 mL min<sup>-1</sup>; sample volume was 1 µL in a splitless mode for 1 min; the temperatures of transfer line and ion source were both 280 °C, respectively; full scan mode was used in the *m/z* range of 30–600 amu. The GC was programmed as follows: initially at 150 °C and held for 5 min, then increased to 280 °C with a ramp rate of 10 °C min<sup>-1</sup> and held for 5 min, finally raised to 300 °C with a ramp rate of 10 °C min<sup>-1</sup> and held for 5 min.

### 3. Results and discussion

#### 3.1. Catalysts characterization

**Fig. 1a** presents the TEM images of NCQDs. The NCQDs with near spherical shape were uniformly distributed. Based on TEM analysis, NCQDs displayed a particle size distribution within 2–7 nm (see **Fig. 1b**). The height of NCQDs was measured by AFM and the results are shown in **Fig. 1c** and d. The accurate heights of NCQDs were below 3 nm based on the analysis results using NanoScope Software 6.13, reflecting that NCQDs consisted of mono- to several layers of graphene. While, p-NCQD-700 had serious agglomeration as shown in **Fig. 1e** and f, likely resulting from calcination at high temperature. More discussion about fluorescence properties and Raman of NCQDs are presented in **Fig. S2** and **Fig. S3**.

The compositions of C, H and N elements in p-NCQD and supported catalysts were determined by elemental analysis and the results are summarized in **Table 1**. p-NCQD had a C content of 55.26 wt.% and N content of 25.21 wt.%. Compared with p-NCQD, p-NCQD-700 presented a higher C content (68.64 wt.%) and a lower N content (22.12 wt.%), due to thermal decomposition of N-containing groups at high treatment temperature. For NCQD(2.49)/SiO<sub>2</sub>-700, NCQD(1.77)/CeZrO<sub>2</sub>-700 and NCQD(2.10)/Al<sub>2</sub>O<sub>3</sub>-700, heat-treatment resulted in N content even below the detection level due to very low loading amounts of NCQDs and the loss of N at high thermal treatment temperature. Moreover, almost identical C contents were identified in the catalysts, i.e., 1.32 wt.% for NCQD(2.49)/SiO<sub>2</sub>-700, 1.38 wt.% for NCQD(1.77)/CeZrO<sub>2</sub>-700, and 1.40 wt.% for NCQD(2.10)/Al<sub>2</sub>O<sub>3</sub>-700, likely due to similar NCQDs loading amounts.

The contents of NCQDs in the supported catalysts were also determined by TG and the results are shown in **Fig. S4**. All samples showed two weight loss peaks. The first weight loss took place below 200 °C, corresponding to the loss of adsorbed water. The second weight

loss was from the decomposition of organic component in the catalyst at around 200–650 °C [42]. The weight loss started at 205.5 °C for NCQD (1.77)/CeZrO<sub>2</sub>-700, 337 °C for NCQD(2.49)/SiO<sub>2</sub>-700 and 362.2 °C for NCQD(2.10)/Al<sub>2</sub>O<sub>3</sub>-700 (results presented in **Fig. S4a**). The low temperature for weight loss in NCQD(1.77)/CeZrO<sub>2</sub>-700 was possibly attributed the strong oxidation capability and mobility of lattice O from CeZrO<sub>2</sub> solid solution. Accordingly, it was previously reported that CeZrO<sub>2</sub> solid solution had a very high catalytic activity in catalytic combustion of organic compounds [43]. The TG curves showed weight losses of 2.49%, 1.77%, and 2.10% for supported NCQDs on SiO<sub>2</sub>, CeZrO<sub>2</sub> and Al<sub>2</sub>O<sub>3</sub>, respectively. As for NCQD(x)/Al<sub>2</sub>O<sub>3</sub>-700 with different NCQDs loading amounts (see **Fig. S4b**), weight losses by 6.28% and 11.88% were observed on NCQD(6.28)/Al<sub>2</sub>O<sub>3</sub>-700 and NCQD (11.88)/Al<sub>2</sub>O<sub>3</sub>-700, respectively.

The XPS analysis were used to determine the surface elemental composition and chemical states of NCQDs on the different supports and the results are presented in **Table 1**, **Fig. S5** and **S6**. For p-NCQD-700, the surface O and N contents were determined to be 6.43 at.% and 15.70 at.%, respectively, much lower than those of p-NCQD (12.25 at.% and 22.23 at.%), indicative of marked loss of O- and N-containing groups upon calcination at 700 °C. On the contrary, the C content increased from 63.13 to 77.04 at.% after calcination at 700 °C due to partial removal of heteroatomic groups (O- and N-containing groups). Accordingly, the C/N ratio of p-NCQD-700 was 4.91, higher than that of p-NCQD (C/N = 2.84). The C/N ratios were 3.16, 4.94 and 9.29 for NCQD(2.49)/SiO<sub>2</sub>-700, NCQD(1.77)/CeZrO<sub>2</sub>-700 and NCQD(2.10)/Al<sub>2</sub>O<sub>3</sub>-700, respectively, much higher than that of p-NCQD (C/N = 2.84). The very different C/N ratios of supported NCQDs were likely correlated to the dispersion of NCQDs on support surface. For NCQD(2.49)/SiO<sub>2</sub>-700 with a special surface area of 21 m<sup>2</sup> g<sup>-1</sup>, NCQDs had a very low dispersion due to the electrostatic repulsive interaction between NCQDs and SiO<sub>2</sub> during the catalyst preparation process, leading to the formation of bulky NCQDs agglomerates (see discussions below), in which the decomposition of N-containing functionalities was effectively inhibited. In contrast, for NCQD(2.10)/Al<sub>2</sub>O<sub>3</sub>-700 with a high special surface area (105 m<sup>2</sup> g<sup>-1</sup>), NCQDs had a very high dispersion because of electrostatic attractive interaction between NCQDs and Al<sub>2</sub>O<sub>3</sub> during the catalyst preparation process. Hence, the majority of N-containing functionalities were exposed, and were liable to decompose upon thermal treatment at high temperature.

Notably, the C1s spectra of all samples were highly asymmetric, implying that the C1s spectra could be divided into multiple peaks. To quantify the species in C1s spectra, the spectra were deconvoluted and the results are presented in **Fig. S5**. The C1s spectra of all samples consisted of multiple species, corresponding to C-C (284.0 ± 0.5 eV), C-N/C-O (285.3 ± 0.2 eV), C = O/C = N (287.0 ± 0.5 eV), and -O-C = O (288.6 ± 0.3 eV), respectively. For p-NCQD, a broad C1s peak was observed, indicative of a high content of C atoms bonded to heteroatoms. In comparison with p-NCQD, p-NCQD-700 had a larger content of aromatic C (i.e., C-C) and a smaller content of C atoms with O/N-containing functionalities (except that in C = O/C = N). For NCQD(2.10)/Al<sub>2</sub>O<sub>3</sub>, the C1s spectrum consisted of four peaks similar to that of p-NCQD. Upon calcination at 700 °C, the content of C-C for NCQD(2.10)/Al<sub>2</sub>O<sub>3</sub>-700 increased from 48.5% to 65.0% and the content of C-O/C-N decreased from 32.8% to 12.6%. Similar trend was observed on both NCQD(1.77)/CeZrO<sub>2</sub>-700 and NCQD(2.49)/SiO<sub>2</sub>-700, indicating that carbonization by thermal treatment led to the formation of cyclized graphite structure and partial removal of heteroatomic functional groups [44]. Moreover, we found that the removal of heteroatomic functional groups and the recovery of graphitic structures were facilitated by increasing the calcination temperature. For example, with the increase of calcination temperature from 500 °C to 700 °C, the content of C-O/C-N in NCQD(2.10)/Al<sub>2</sub>O<sub>3</sub>-y decreased from 30.8% to 12.6%, and C-C content increased from 43.9% to 65.0% (**Fig. S5**). Notably, carbonization of NCQDs at 700 °C led to slightly increased contents of C = O/C = N, likely due to the conversion of carboxyl to

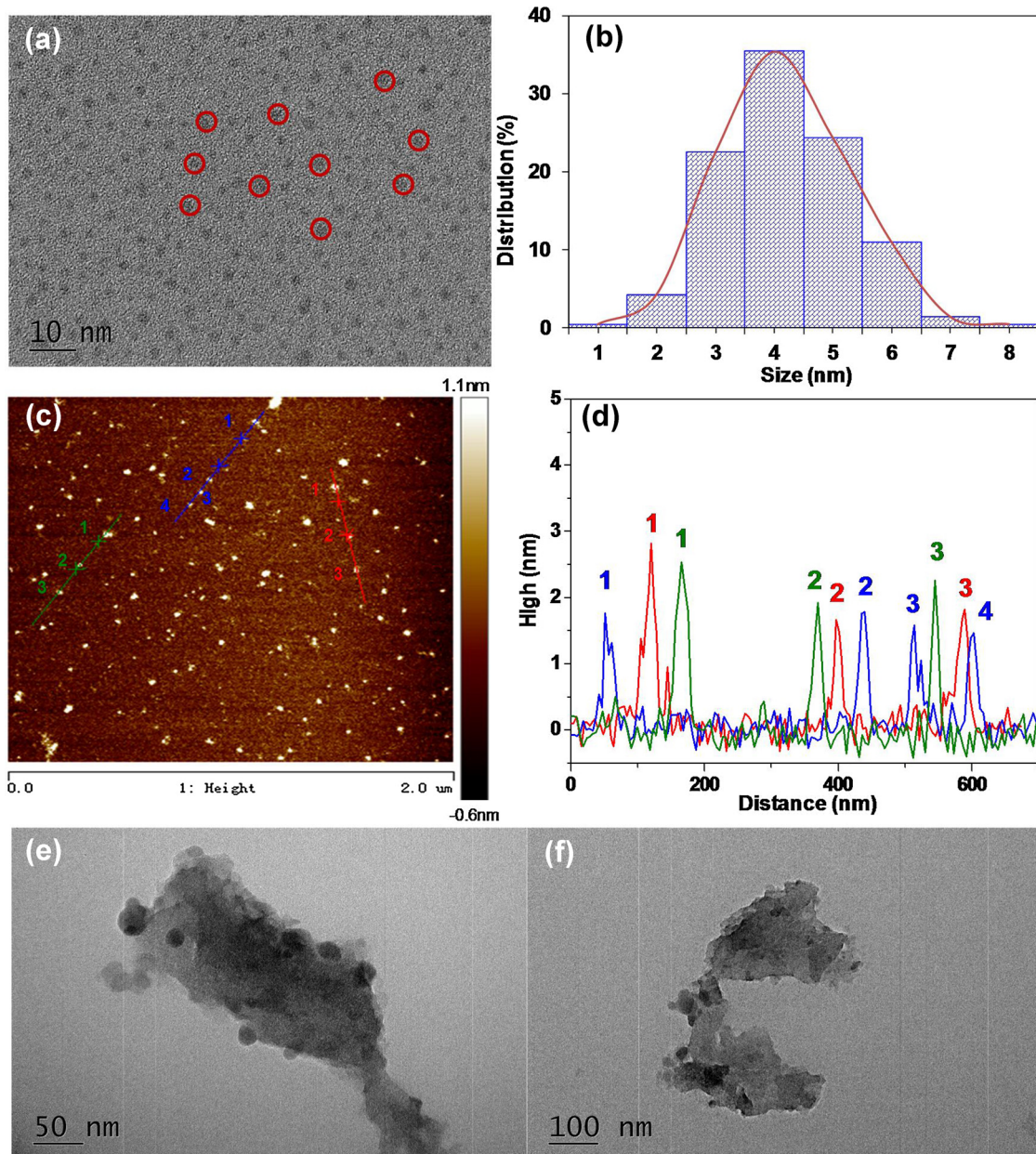


**Fig. 1.** (a) TEM image and (b) the corresponding size distribution of NCQDs. (c) AFM image and (d) the corresponding height distribution of NCQDs. (e),(f) TEM images of p-NCQD-700.

carbonyl carbon [45].

Similarly, N1s spectra of the catalysts contained multiple species and were deconvoluted. The results are compiled in Fig. S6. All samples consisted of three nitrogen species, i.e., pyridinic, pyrrolic and graphitic

N with binding energy at  $398.8 \pm 0.2$  eV,  $400 \pm 0.2$  eV, and  $401.5 \pm 0.2$  eV, respectively. Calcination of p-NCQD at  $700^\circ\text{C}$  led to the decrease of N content from 22.23 at.% to 15.70 at.% due to decomposition of N-containing groups at high temperature. Additionally,

**Table 1**  
Chemical compositions of NCQDs and specific surface area ( $S_{\text{BET}}$ ) of catalysts.

Sample	XPS (at.%)				Elemental analysis (wt.%)				$S_{\text{BET}}$ ( $\text{m}^2 \text{g}^{-1}$ )
	C	O	N	C/N	C	H	N	C/N	
p-NCQD	63.13	12.25	22.23	2.84	55.26	3.25	25.21	2.19	/
p-NCQD-700	77.04	6.43	15.70	4.91	68.64	1.73	22.12	3.10	/
NCQD(2.49)/SiO <sub>2</sub> -700	5.06	63.56	1.60	3.16	1.32	1.03	BDL <sup>a</sup>	/	21
NCQD(1.77)/CeZrO <sub>2</sub> -700	47.19	33.31	9.56	4.94	1.38	0.33	BDL	/	19
NCQD(2.10)/Al <sub>2</sub> O <sub>3</sub> -700	26.76	42.89	2.88	9.29	1.40	0.80	BDL	/	105
NCQD(2.10)/Al <sub>2</sub> O <sub>3</sub>	21.57	43.42	7.63	2.83	3.26	0.78	1.21	2.69	108

<sup>a</sup> Below detection limit.

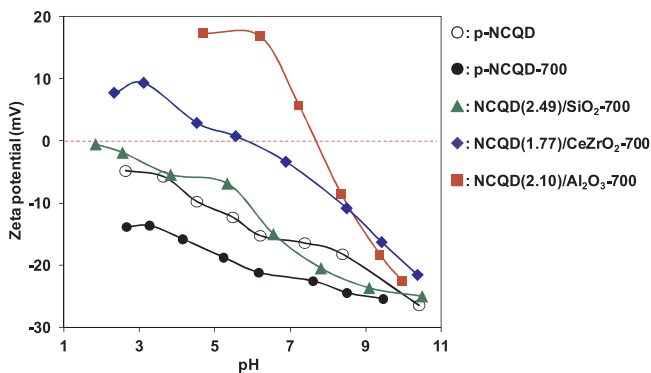


Fig. 2. Zeta potentials of the catalysts as a function of pH.

the contents of graphitic N were found to be markedly increased from 6.3% (p-NCQD) to 27.6%, 28.4%, 24.1% and 25.1% in p-NCQD-700, NCQD(2.10)/Al<sub>2</sub>O<sub>3</sub>-700, NCQD(1.77)/CeZrO<sub>2</sub>-700 and NCQD(2.49)/SiO<sub>2</sub>-700, respectively. The much higher graphitic N contents in the calcined catalysts than that in p-NCQD were attributed to conversion of pyridinic and pyrrolic N to graphitic N due to the higher stability of graphitic N than other N species at high temperature [46,47].

The surface zeta potentials of the samples were determined as a function of pH, and the results are presented in Fig. 2. For supported NCQDs, the IEPs were found to be < 2.0, 5.8 and 7.6 for NCQD(2.49)/SiO<sub>2</sub>-700, NCQD(1.77)/CeZrO<sub>2</sub>-700 and NCQD(2.10)/Al<sub>2</sub>O<sub>3</sub>-700, respectively, which were approximately identical to those of the supports shown in Fig. S7 (i.e., 2.4 for SiO<sub>2</sub>, 6.2 for CeZrO<sub>2</sub>, and 8.1 for Al<sub>2</sub>O<sub>3</sub>). Under reaction conditions (pH = 6.4), the zeta potential of NCQD(2.10)/Al<sub>2</sub>O<sub>3</sub>-700 was 14 mV, much higher than those of NCQD(2.49)/SiO<sub>2</sub>-700 (-15 mV) and NCQD(1.77)/CeZrO<sub>2</sub>-700 (-2 mV), probably because of the strong basicity of surface hydroxyl groups of Al<sub>2</sub>O<sub>3</sub>. The surface zeta potentials of p-NCQD and p-NCQD-700 remained negative in the test pH range of 2–10, likely due to the presence of large quantities of oxygen-containing groups on the surface as indicated by XPS analysis.

To investigate the distribution of NCQDs on supports, HAADF-STEM mapping was carried out and the resulting images are compiled in

Fig. 3. The presence of C and N in the supported catalysts revealed that NCQDs were successfully loaded on support surface. In terms of the distribution image of C element, however, the dispersion of NCQDs varied with supports. For NCQD(2.10)/Al<sub>2</sub>O<sub>3</sub>-700 and NCQD(1.77)/CeZrO<sub>2</sub>-700 (see Fig. 3a and c), C element was homogeneously distributed on supports surface, while for NCQD(2.49)/SiO<sub>2</sub>-700 (see Fig. 3b), C element was accumulated at the edge of SiO<sub>2</sub>, reflecting marked agglomeration of NCQDs on SiO<sub>2</sub> surface. Clearer conclusion could be obtained on the element images of C + Al, C + Ce + Zr and Si + C. Overlapping of C element with Al and (Ce + Zr) elements was visible on both NCQD(2.10)/Al<sub>2</sub>O<sub>3</sub>-700 and NCQD(1.77)/CeZrO<sub>2</sub>-700, confirming the high dispersion of NCQDs on Al<sub>2</sub>O<sub>3</sub> and CeZrO<sub>2</sub>. On the contrary, Si element was covered by a thick layer of C element accumulated on the edge of Si element, clearly reflecting that NCQDs aggregated on SiO<sub>2</sub> surface. Such very different dispersions of NCQDs on three supports could be well explained by IEPs of supports and NCQDs. As zeta potential measurement indicated, NCQDs were negatively charged under catalyst preparation conditions due to its very high content of O-containing functionalities. Al<sub>2</sub>O<sub>3</sub> and CeZrO<sub>2</sub> were positively charged in the impregnating solution at pH 6.0 due to their high IEPs (8.1 for Al<sub>2</sub>O<sub>3</sub>, and 6.2 for CeZrO<sub>2</sub>), which invoked electrostatic attractive interactions between NCQDs and Al<sub>2</sub>O<sub>3</sub> and CeZrO<sub>2</sub>, resulting in high dispersions of NCQDs on the supports during the catalyst preparation process. In contrast, SiO<sub>2</sub> was negatively charged, and electrostatic repulsive interactions occurred between NCQDs and SiO<sub>2</sub>, leading to agglomeration of NCQDs on SiO<sub>2</sub> surface.

The XRD patterns of p-NCQD and p-NCQD-700 are shown in Fig. S8. For p-NCQD, two peaks were observed at around 26.5° and 44° characteristic of (002) and (010) diffractions from graphite phase, respectively [48–50]. As for p-NCQD-700, stronger (002) peak was observed, likely due to agglomeration of NCQDs during the carbonization process [51,52]. For supported NCQDs on SiO<sub>2</sub>, CeZrO<sub>2</sub> and Al<sub>2</sub>O<sub>3</sub>, the characteristic peaks of NCQDs were absent in XRD patterns (see results in Fig. S8b, 8c, and 8d), owing to low NCQDs loading amounts or/and effective dispersion of NCQDs on the supports.

### 3.2. Activation of PDS for BPF degradation on supported NCQDs catalysts

The degradation of BPF on supported catalysts is compiled in

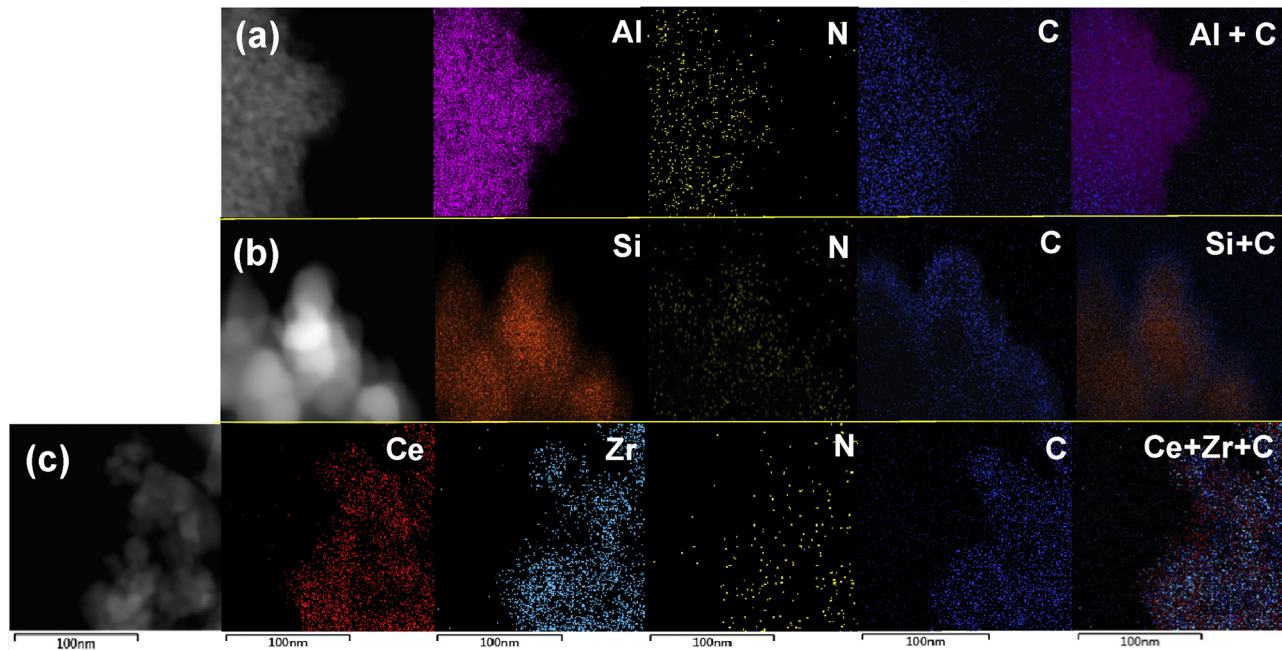
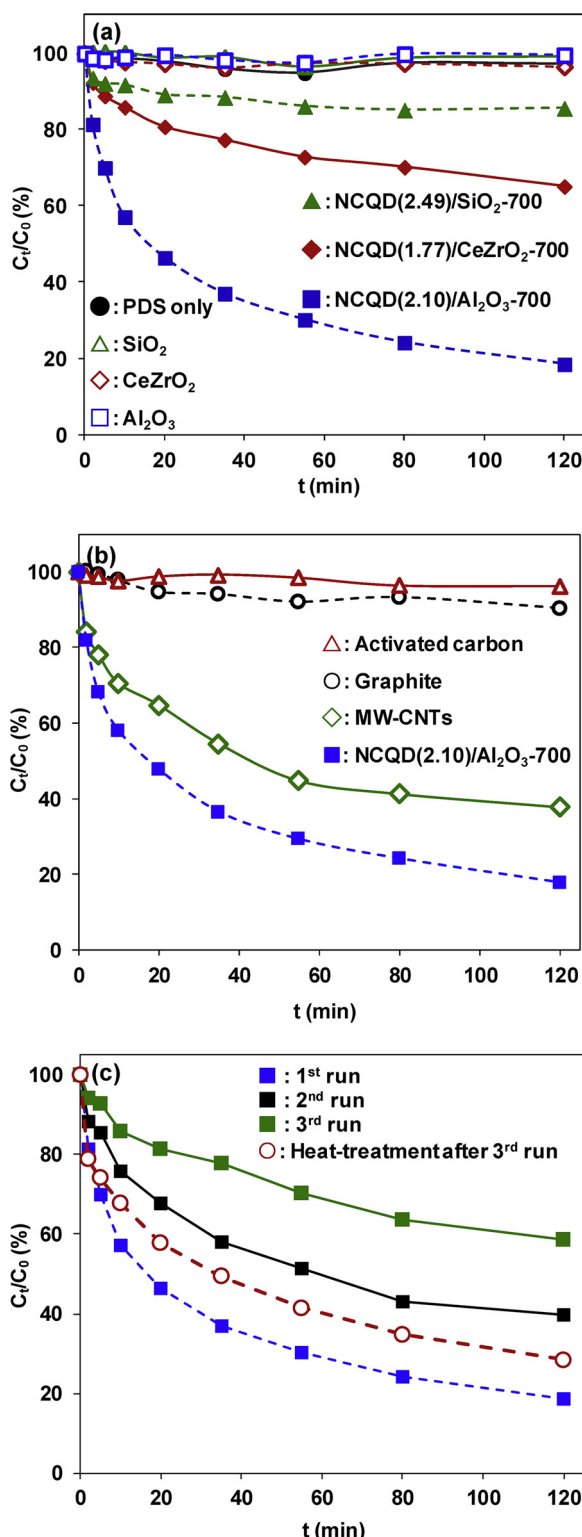


Fig. 3. Dark-field STEM images and corresponding elemental STEM mapping images of (a) NCQD(2.10)/Al<sub>2</sub>O<sub>3</sub>-700, (b) NCQD(2.49)/SiO<sub>2</sub>-700 and (c) NCQD(1.77)/CeZrO<sub>2</sub>-700.



**Fig. 4.** Removal of BPF on (a) supported NCQDs catalysts, (b) commercial carbons, and (c) reused and restored NCQD(2.10)/Al<sub>2</sub>O<sub>3</sub>-700. Reaction conditions: 1 mM PDS, 0.1 mM BPF, and 0.25 g L<sup>-1</sup> catalyst at 25 °C and pH 6.4.

**Fig. 4a.** In the absence of catalysts, a negligible BPF removal of 2.8% within 120 min was observed. Similarly, the presence of  $\text{SiO}_2$ ,  $\text{CeZrO}_2$  and  $\text{Al}_2\text{O}_3$  resulted in BPF removal below 5% within 120 min, indicative of negligible catalytic activities of the supports. In contrast, BPF was degraded within 120 min by 14.3%, 34.9% and 81.5% on  $\text{NCQD}(2.49)/\text{SiO}_2$ -700,  $\text{NCQD}(1.77)/\text{CeZrO}_2$ -700 and  $\text{NCQD}(2.10)/\text{Al}_2\text{O}_3$ -700,

respectively, indicating that carbonized NCQDs loaded on support surface were the main activity sites for PDS activation. The surface defects, graphitic structure and N-containing functionalities of carbonized NCQDs could act as the catalytic active sites for PDS activation [26,29,32,33]. The results also showed that supported NCQDs catalysts on different supports presented significantly different catalytic activities. Supported NCQDs on  $\text{Al}_2\text{O}_3$  catalyst exhibited much higher catalytic activity for BPF degradation than other supported catalysts. In a heterogeneous catalysis process, adsorption of reactants on the catalyst surface played a crucial role [53–55]. In parallel, the IEPs of NCQD(2.49)/ $\text{SiO}_2$ -700, NCQD(1.77)/ $\text{CeZrO}_2$ -700 and NCQD(2.10)/ $\text{Al}_2\text{O}_3$ -700 were determined to be < 2.0, 5.8 and 7.6, respectively. Considering that PDS presented in an anionic form, therefore, electrostatic repulsive interactions could be expected between PDS and NCQD(2.49)/ $\text{SiO}_2$ -700 and NCQD(1.77)/ $\text{CeZrO}_2$ -700 at the reaction pH of 6.4, whereas electrostatic attractive interactions existed between PDS and NCQD(2.10)/ $\text{Al}_2\text{O}_3$ -700. Hence, more efficient adsorption and activation of PDS on NCQD(2.10)/ $\text{Al}_2\text{O}_3$ -700 could be expected than on NCQD(2.49)/ $\text{SiO}_2$ -700 and NCQD(1.77)/ $\text{CeZrO}_2$ -700. Despite of repulsive interactions between PDS and both NCQD(2.49)/ $\text{SiO}_2$ -700 and NCQD(1.77)/ $\text{CeZrO}_2$ -700, the zeta potential of NCQD(2.49)/ $\text{SiO}_2$ -700 at pH of 6.4 was more negative (see Fig. 2), invoking stronger repulsive interactions than NCQD(1.77)/ $\text{CeZrO}_2$ -700. As a result, a lower catalytic activity was observed on NCQD(2.49)/ $\text{SiO}_2$ -700 than on NCQD(1.77)/ $\text{CeZrO}_2$ -700. Additionally, the uniform distribution of NCQDs on the surface of catalyst (see HAADF-STEM mapping results) contributed to the higher catalytic activity of supported NCQDs on  $\text{Al}_2\text{O}_3$  and  $\text{CeZrO}_2$  than on  $\text{SiO}_2$ . Similarly, Chen et al. [56] studied the effect of different supports (i.e.,  $\text{SiO}_2$ ,  $\text{Al}_2\text{O}_3$  and activated carbon) on the liquid phase catalytic hydrogenation of bromate on supported Pd catalysts, and concluded that the low catalytic activities of Pd catalysts supported on  $\text{SiO}_2$  and activated carbon were mainly attributed to the electrostatic repulsive interaction between bromate and catalysts, which suppressed bromate adsorption on catalyst surface. Fig. 4b compares the catalytic BPF degradation kinetics over NCQD(2.10)/ $\text{Al}_2\text{O}_3$ -700 with that over several commercial carbons. At the same catalyst dosage, activated carbon and graphite exhibited poor catalytic activities with 3.8% and 9.5% of BPF removal within 120 min. MW-CNT showed moderate catalytic activity with 62.3% of BPF removal in 120 min, which was still below the catalytic activity of NCQD(2.10)/ $\text{Al}_2\text{O}_3$ -700 (81.5%). We further compared BPF degradation efficiency reported in similar studies (listed in Table S2). The results showed that NCQD(2.10)/ $\text{Al}_2\text{O}_3$ -700 was a very effective metal free catalyst for PDS activation.

Similar to other carbonaceous catalysts [26,30,32], catalyst deactivation was observed on NCQD(2.10)/ $\text{Al}_2\text{O}_3$ -700 (results presented in Fig. 4c). After three cycles, BPF removal decreased from 81.5% to 41.3% within 120 min. Characterization of the reused catalyst by HAADF-STEM mapping showed that carbonized NCQDs particles were stable without marked agglomeration during the catalytic process (results presented in Fig. S9). Hence, the deactivation of the catalyst was mainly due to the oxidation of NCQDs during PDS activation process. Accordingly, similar deactivation due to surface oxidation was also observed on carbonaceous catalysts [30,37]. However, the catalytic activity of NCQD(2.10)/ $\text{Al}_2\text{O}_3$ -700 could be substantially restored by calcination under  $\text{N}_2$  atmosphere at 400 °C for 1 h.

### 3.3. Influence of calcination temperature on catalytic activity of NCQDs

The effect of calcination temperature of p-NCQD-y and NCQD(2.10)/ $\text{Al}_2\text{O}_3$ -y catalysts on PDS activation for BPF degradation is presented in Fig. 5. For p-NCQD-y catalysts, the removal of BPF was below 4% after reaction for 120 min, indicative of a very low catalytic activity. However, much higher catalytic activities were observed on supported NCQDs catalysts and the catalytic activities of the NCQD(2.10)/ $\text{Al}_2\text{O}_3$ -y catalysts differed with calcination temperature. For example, the removal of BPF within 120 min was 9.4%, 46.3% and 81.5% on NCQD

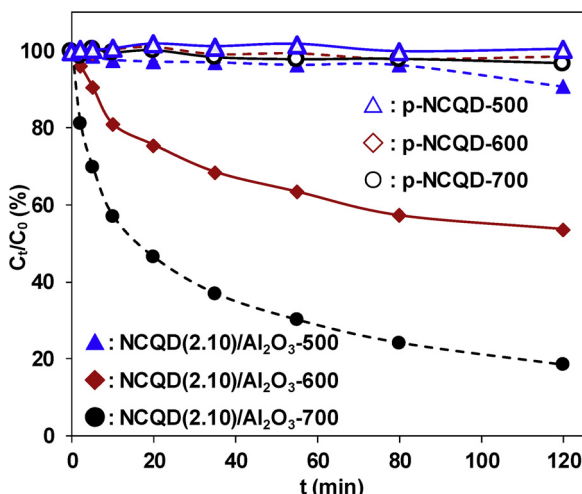


**Fig. 5.** Effect of carbonization temperature on BPF degradation over p-NCQD-y and NCQD(2.10)/Al<sub>2</sub>O<sub>3</sub>-y. Reaction conditions: 1 mM PDS, 0.1 mM BPF, and 0.25 g L<sup>-1</sup> catalyst at 25 °C and pH 6.4.

(2.10)/Al<sub>2</sub>O<sub>3</sub>-500, NCQD(2.10)/Al<sub>2</sub>O<sub>3</sub>-600 and NCQD(2.10)/Al<sub>2</sub>O<sub>3</sub>-700, respectively, reflecting an enhanced catalytic activity with calcination temperature. In comparison with p-NCQD-y catalysts, the very high catalytic activities of the NCQD(2.10)/Al<sub>2</sub>O<sub>3</sub>-y catalysts could be attributed to more exposed active sites from highly dispersed NCQDs, as reflected by HAADF-STEM mapping results. Furthermore, the supported NCQDs on Al<sub>2</sub>O<sub>3</sub> catalysts had higher IEPs than p-NCQD-700, facilitating PDS adsorption and activation and thus resulting in enhanced BPF degradation. As for the impact of calcination, the increase of calcination temperature favored the removal of heteroatomic functional groups and the recovery of graphitic structures (see XPS data, Fig. S5). Thus, the catalytic activity of NCQD(2.10)/Al<sub>2</sub>O<sub>3</sub>-y catalyst for PDS activation increased with increasing calcination temperature.

#### 3.4. Influence of NCQDs loading amount on PDS activation

Because NCQDs acted as the active sites for PDS activation, increasing NCQDs loading was expected to improve BPF degradation. The effect of NCQDs loading amount of the catalysts on PDS degradation is illustrated in Fig. 6a. The degradation of BPF was improved from 81.5% to 98.7% with the increase of NCQDs loading amount from 2.10% to 6.28%, while further increasing NCQDs loading amount to 11.88% led to decreased BPF degradation to 79.8%. In parallel, the initial activities, which were calculated within initial 5 min to avoid the interferences caused by the competitive adsorption of degradation intermediates or products, were 0.023, 0.033 and 0.018 mmol gCat<sup>-1</sup> min<sup>-1</sup> for the catalysts with NCQDs loading amounts of 2.10%, 6.28% and 11.88%, respectively, displaying a volcano-type dependency (see Fig. 6b). At low NCQDs loadings, the enhanced activity of the catalyst with the increase of NCQDs loading could be ascribed to increased active sites, whereas further increasing loading likely resulted in NCQDs agglomeration on Al<sub>2</sub>O<sub>3</sub> surface and decreased active sites, suppressing BPF degradation. Clearer conclusion could be obtained by normalizing the initial activity by NCQDs loading amount. The normalized activities by NCQDs loading were calculated to be 1.12, 0.52 and 0.15 mmol gNCQDs<sup>-1</sup> min<sup>-1</sup> for NCQD(2.10)/Al<sub>2</sub>O<sub>3</sub>-700, NCQD(6.28)/Al<sub>2</sub>O<sub>3</sub>-700 and NCQD(11.88)/Al<sub>2</sub>O<sub>3</sub>-700, respectively, reflecting a decreased activity with NCQDs loading from 2.10% to 11.88%. Such a negative impact of NCQDs loading on normalized catalytic activity was attributed to the gradual agglomeration of NCQDs on Al<sub>2</sub>O<sub>3</sub> surface with the increase of loading amount. Notably, the normalized initial activity of NCQD(2.10)/Al<sub>2</sub>O<sub>3</sub>-700 was even more than twice as high as that of NCQD(6.28)/Al<sub>2</sub>O<sub>3</sub>-700, clearly indicative the crucial importance of

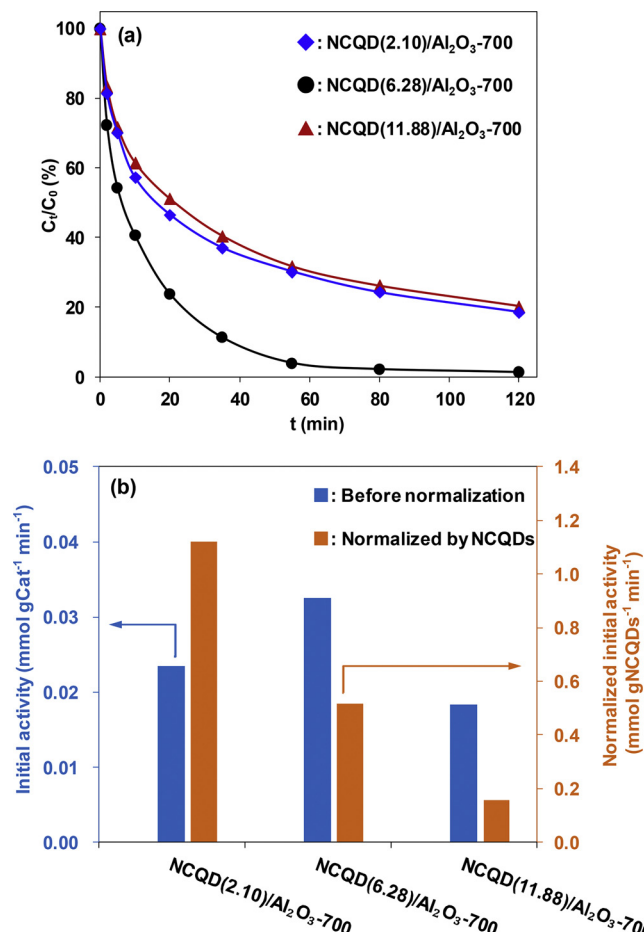


**Fig. 6.** Effect of NCQDs loading amount on BPF degradation by PDS over NCQD(x)/Al<sub>2</sub>O<sub>3</sub>-700. (a) Degradation kinetics and (b) the corresponding initial activity within initial 5 min. Reaction conditions: 1 mM PDS, 0.1 mM BPF, and 0.25 g L<sup>-1</sup> catalyst at 25 °C and pH 6.4.

high dispersion of NCQDs on Al<sub>2</sub>O<sub>3</sub> surface.

#### 3.5. Influence of initial concentration of PDS and BPF on BPF degradation

For a heterogeneous catalytic reaction, reactants adsorption on catalyst surface is commonly a prerequisite step. To further verify the mechanism of PDS activation and BPF degradation on NCQD(2.10)/Al<sub>2</sub>O<sub>3</sub>-700, the impacts of the initial concentrations of BPF and PDS on BPF degradation were investigated and the results are shown in Fig. 7. At a fixed initial PDS concentration of 1 mM, the initial activity continuously increased from 0.0099 to 0.025 mmol gCat<sup>-1</sup> min<sup>-1</sup> with the increase of initial BPF concentration from 0.025 to 0.15 mM (see Fig. 7a and b). Further increasing initial BPF concentration to 0.25 mM led to almost identical initial activity around 0.025–0.023 mmol gCat<sup>-1</sup> min<sup>-1</sup>, reflecting that maximum BPF adsorption amount reached. In parallel, the influence of initial PDS concentration on BPF degradation is presented in Fig. 7c and d with initial BPF concentration fixed at 0.1 mM. Again, increasing initial PDS concentration from 0.08 to 0.5 mM led to the increase of initial BPF degradation rate from 0.0098 to 0.021 mmol gCat<sup>-1</sup> min<sup>-1</sup>. However, further increase of PDS concentration from 0.5 to 2 mM resulted in almost stable BPF degradation rate ranging from 0.021 to 0.025 mmol gCat<sup>-1</sup> min<sup>-1</sup>. The impacts of initial concentrations of PDS and BPF on BPF degradation were further fitted to the binary Langmuir-Hinshelwood model. For BPF degradation with varied initial BPF and PDS concentrations, the degradation rate was described as follows [58],

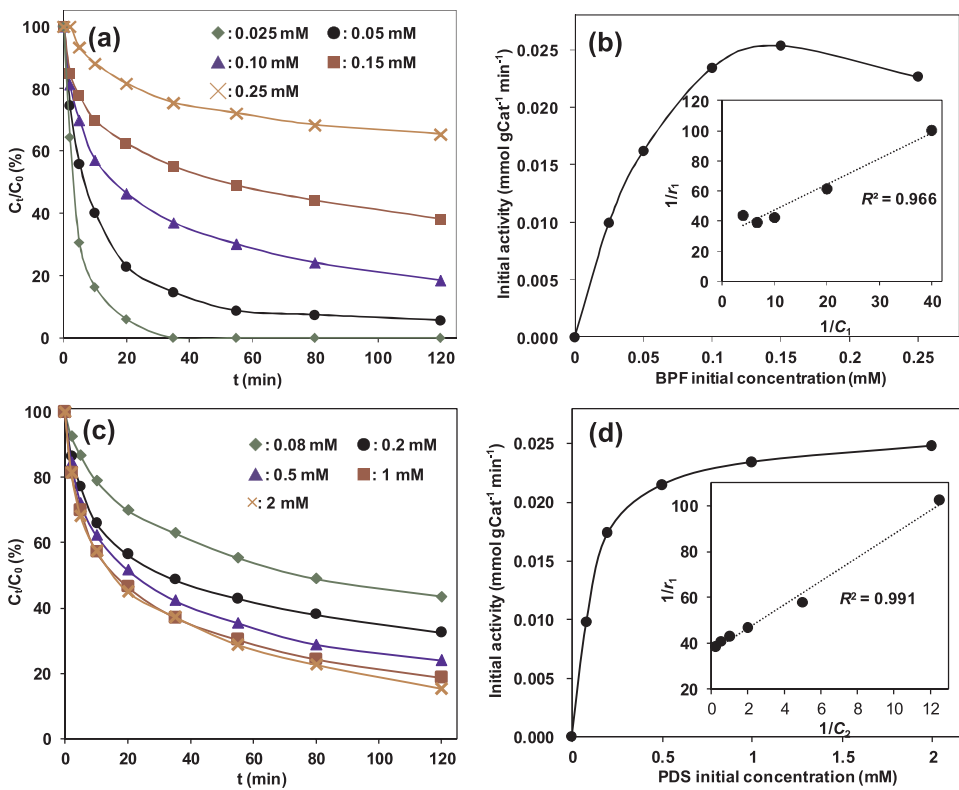


**Fig. 7.** Effect of (a),(b) initial BPF concentrations and (c),(d) initial PDS concentrations on BPF degradation by PDS over NCQD(2.10)/Al<sub>2</sub>O<sub>3</sub>-700. (a),(c) Degradation kinetics and (b),(d) the corresponding initial activity within initial 5 min. Reaction conditions: (a),(b) 0.025~0.25 mM BPF and 1 mM PDS or (c),(d) 0.1 mM BPF and 0.08~2 mM PDS, 0.25 g L<sup>-1</sup> catalyst at 25 °C and pH 6.4.

$$r_1 = k\theta_s = k \frac{b_1 C_1}{1 + b_1 C_1 + b_2 C_2} \quad (1)$$

$$\frac{1}{r_1} = \frac{1}{kb_1 C_1} + \frac{1}{k} + \frac{b_2 C_2}{kb_1 C_1} \quad (2)$$

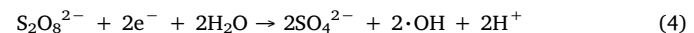
where  $r_1$  is the initial degradation rate of BPF,  $C_1$  is the initial BPF concentration,  $C_2$  is the initial PDS concentration,  $\theta_s$  is the surface coverage of BPF adsorption,  $k$  is the reaction rate constant, and  $b_1$  and  $b_2$  are the adsorption constants of BPF and PDS, respectively.

Langmuir-Hinshelwood model assumes that the reaction rate is proportional to the concentration of adsorbed reactant, and the conversion of adsorbed reactants on catalyst surface is the rate controlling step. The plot of  $1/r_1$  versus  $1/C_1$  gave a good linear relationship with  $R^2$  larger than 0.96, respectively, indicating that the degradation of BPF via PDS activation could be well described using the Langmuir-Hinshelwood model (see Fig. 7b and inset), confirming that the adsorbed BPF on catalyst surface was the rate controlling step. In parallel, for BPF degradation with varied initial PDS concentrations at fixed initial BPF concentration, a good linear relationship ( $R^2$  above 0.99) was also obtained in the plot of  $1/r_1$  versus  $1/C_2$  (see Fig. 7d and inset), indicative of the crucial role of adsorbed PDS for BPF degradation.

### 3.6. Role of reactive radicals in BPF degradation

EPR was employed to identify the reactive radicals produced by catalytic PDS activation on NCQD(2.10)/Al<sub>2</sub>O<sub>3</sub>-700, and the spectra are illustrated in Fig. 8a. The 5,5-dimethyl-1-pyrroline (DMPO) was used as the radical spin trapping agent for trapping SO<sub>4</sub><sup>·-</sup> and ·OH [30,59], and 2,2,6,6-tetramethyl-4-piperidone (TEMP) for singlet oxygen (<sup>1</sup>O<sub>2</sub>) [60]. In the presence of DMPO, very strong peaks with intensity ratio of 1:2:2:1 were observed, characteristic of the DMPO-OH adduct with hyperfine splitting constants of  $a_N = a_H = 14.9$  G. The ·OH was generated from the oxidation of water under the coexistence of PDS and NCQD(2.10)/Al<sub>2</sub>O<sub>3</sub>-700 [30]. Similarly, the ·OH production was identified in catalytic PDS activation by many other carbon-based

materials (e.g., N-doped single-walled carbon nanotubes, reduced graphene oxides, and nanodiamonds) [30,31,57]. Additionally, weak signals with hyperfine splitting constants of  $a_N = 13.2$  G,  $a_H = 9.6$  G,  $a_H = 1.48$  G, and  $a_H = 0.78$  G were identified, ascribed to DMPO-SO<sub>4</sub> adduct [61]. The presence of DMPO-OH and DMPO-SO<sub>4</sub> was indicative of the formation SO<sub>4</sub><sup>·-</sup> and ·OH in the NCQD(2.10)/Al<sub>2</sub>O<sub>3</sub>-700/PDS system. In contrast, in the presence of TEMP no visible signals were observed, indicative of the absence of <sup>1</sup>O<sub>2</sub> in the NCQD(2.10)/Al<sub>2</sub>O<sub>3</sub>-700/PDS system. Based on the EPR spectra and PDS activation mechanism [30,31], the activation process of PDS on NCQD(2.10)/Al<sub>2</sub>O<sub>3</sub>-700 was described in Eqs. (3) and (4).



To further investigate the contribution of SO<sub>4</sub><sup>·-</sup> and ·OH to BPF degradation, we examined the reaction in the presence of two radical scavengers, methanol and *tert*-butanol, and the results are compiled in Fig. 8b. Methanol is a scavenger of both SO<sub>4</sub><sup>·-</sup> and ·OH, having a reaction rate of  $2.5 \times 10^7$  M<sup>-1</sup> s<sup>-1</sup> with SO<sub>4</sub><sup>·-</sup> and a rate  $9.7 \times 10^8$  M<sup>-1</sup> s<sup>-1</sup> with ·OH [62–64]. *tert*-Butanol was also used as a radical scavenger, for quenching ·OH with a high rate constant of  $3.8\text{--}7.6 \times 10^8$  M<sup>-1</sup> s<sup>-1</sup>, but quenching SO<sub>4</sub><sup>·-</sup> with a much lower rate constant of  $4.0\text{--}9.1 \times 10^5$  M<sup>-1</sup> s<sup>-1</sup> [63]. In comparison with BPF degradation without radical scavengers, the presence of 1 M methanol and *tert*-butanol led to decreased BPF removal from 81.5% to 69.0% and to 76.4% within 120 min, respectively, due to effectively quenching SO<sub>4</sub><sup>·-</sup> and ·OH by methanol and *tert*-butanol. Additionally, increasing methanol concentration to 5 M further inhibited BPF degradation with a much low degradation removal of 17.2%, confirming that SO<sub>4</sub><sup>·-</sup> and ·OH were the main active species for BPF degradation upon PDS activation on NCQD(2.10)/Al<sub>2</sub>O<sub>3</sub>-700.

### 3.7. Degradation pathways of BPF

In the catalyst/PDS system, ·OH and SO<sub>4</sub><sup>·-</sup> were the main active

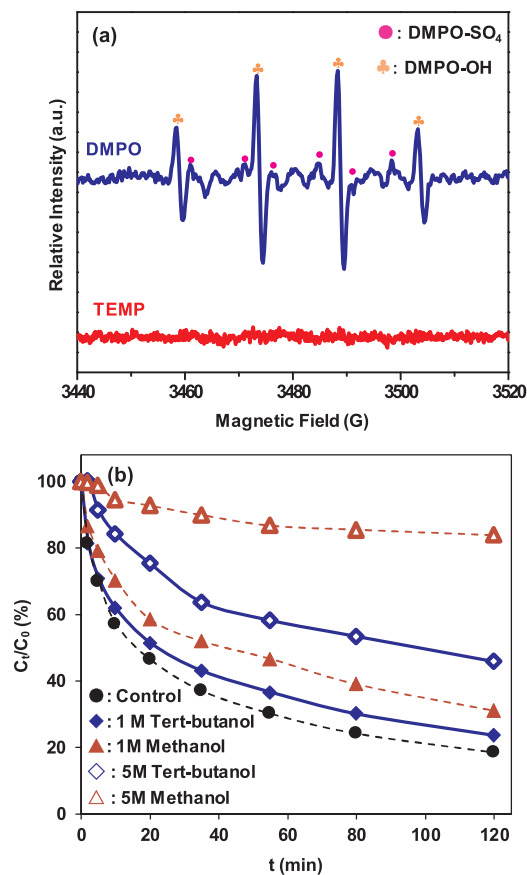


**Fig. 8.** (a) EPR spectra of catalytic PDS activation on NCQD(2.10)/Al<sub>2</sub>O<sub>3</sub>-700 using DMPO and TEMP as the radical spin trapping agents. Reaction conditions: 100 mM DMPO or TEMP, 1 mM PDS and 0.25 g L<sup>-1</sup> catalyst in 100 mM phosphate buffer (pH 7.4) for 10-min reaction. (b) Effect of different radical scavengers on BPF degradation over NCQD(2.10)/Al<sub>2</sub>O<sub>3</sub>-700. Reaction conditions: 1 mM PDS, 0.1 mM BPF, and 0.25 g L<sup>-1</sup> catalyst at 25 °C and pH 6.4.

species and may lead to different reaction pathways for BPF degradation. Generally, ·OH attacks organics via three ways, i.e., electron transfer, addition, or hydrogen abstraction [65]. In contrast, SO<sub>4</sub><sup>·-</sup> reacts with benzene-containing compounds mainly via electron transfer. The degradation of BPF by photochemistry [66], bacteria [67]

and chemical oxidation [68] has been previously reported. However, little attention was played on the degradation of BPF in the coexistence of ·OH and SO<sub>4</sub><sup>·-</sup>, which might produce varied intermediates through different degradation pathways due to the unique reaction mechanisms of ·OH and SO<sub>4</sub><sup>·-</sup>. Hence, the degradation intermediates of BPF in the NCQD(2.10)/Al<sub>2</sub>O<sub>3</sub>-700/PDS system were identified by GC-MS after extraction and silylation. The total ion chromatography (TIC) spectra of trimethylsilyl (TMS) derivatives with different degradation time are presented in Fig. S10. Only one peak was observed at 15.89 min with *m/z* of 344, ascribed to silylated BPF with characteristic fragments (*m/z*) of 344, 329, 179 [69]. After degradation for 60 min, seven intermediates peaks were observed at retention time of 7.60 (P4), 7.68 (P3), 8.95 (P2), 10.47 (P5), 16.96 (P7), 17.92 (P6) and 18.85 (P1) min. Based on corresponding extracted ion chromatogram (XIC) and the principal fragment peaks in Fig. S11, the seven intermediates were assigned and the detail information are listed in Table 2. After reaction for 200 min, the peaks of silylated BPF, P1, P6, and P7 were disappeared, leaving oxidation products (P2, P3, P4, P5). Based on the GC-MS data, two possible degradation pathways were proposed in Fig. 9. One of the degradation pathway was started with the attack of SO<sub>4</sub><sup>·-</sup> via breaking C-C bond (the red dotted line), producing intermediates of P1 and P2, which was similar to the degradation of BPA via photocatalytic [70] and ultrasonic [71]. Then, P1 was hydroxylated to P3 and P2 was further oxidized into P4 and then P5. Another degradation pathway was initialized from the hydroxylation of BPF via adducting ·OH, resulting in P6 and P7. Eventually BPF and all intermediates were capable of being mineralized to CO<sub>2</sub> and H<sub>2</sub>O under continuous reaction in the NCQD(2.10)/Al<sub>2</sub>O<sub>3</sub>-700/PDS system. In line with this, 71.2% of the TOC in the reaction system was removed after the 120 min reaction (Fig. S12).

#### 4. Conclusion

In the present study, supported NCQDs on three different supports (e.g., SiO<sub>2</sub>, CeZrO<sub>2</sub> and γ-Al<sub>2</sub>O<sub>3</sub>) were prepared and liquid phase catalytic PDS activation on the catalysts for BPF degradation was investigated. Characterization results show that NCQDs are highly dispersed on Al<sub>2</sub>O<sub>3</sub> and CeZrO<sub>2</sub> due to strong electrostatic attractive interaction between NCQDs and the supports, whereas NCQDs are aggregated on SiO<sub>2</sub>, resulting from repulsive interaction between NCQDs and SiO<sub>2</sub>. Upon thermal treatment, heteroatomic groups of NCQDs in the catalysts are effectively removed. NCQDs supported on Al<sub>2</sub>O<sub>3</sub> exhibit much higher catalytic activity than on SiO<sub>2</sub> and CeZrO<sub>2</sub>, attributed to its stronger PDS adsorption. Accordingly, the influences of

**Table 2**  
Intermediates (P1-P7) during the degradation of BPF.

Intermediates	Retention time (min)	Molecular weight of TMS derivatives ( <i>m/z</i> )	Characteristic fragments ( <i>m/z</i> )	Molecular structure
BPF	15.89	344	344, 329, 179	
phenol (P1)	18.85	166	166, 151	
<i>p</i> -hydroxybenzyl alcohol (P2)	8.95	268	268, 258, 237	
hydroquinone (P3)	7.68	254	254, 239, 112	
<i>p</i> -hydroxybenzaldehyde (P4)	7.60	194	194, 151, 133	
<i>p</i> -hydroxybenzoic acid (P5)	10.47	282	282, 267, 223, 193	
3,3',4,4'-tetrahydroxydiphenylmethane (P6)	17.92	520	520, 431, 267, 207	
trihydroxydiphenylmethane (P7)	16.96	432	432, 417, 223, 135	

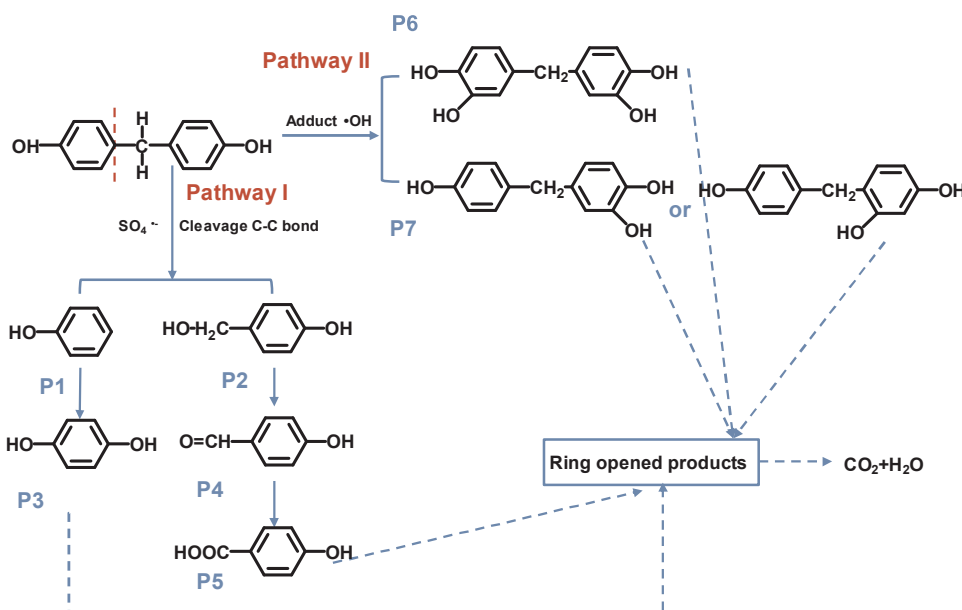


Fig. 9. Proposed degradation pathways of BPF in the NCQD(2.10)/Al<sub>2</sub>O<sub>3</sub>-700/PDS system.

initial concentrations of PDS and BPF on catalytic activity of NCQD(2.10)/Al<sub>2</sub>O<sub>3</sub>-700 indicate that BPF degradation can be well described using the binary Langmuir-Hinshelwood model, reflecting that the adsorption of PDS and BPF is the rate-controlling step. Increasing thermal treatment temperature of NCQD(2.10)/Al<sub>2</sub>O<sub>3</sub>-y results in enhanced BPF degradation, which is attributed to the effective carbonization and removal of O-functionalities of NCQDs. Additionally, BPF degradation is closely related to the loading amount of NCQDs on Al<sub>2</sub>O<sub>3</sub>, displaying a volcano-type dependency of the catalytic activity on NCQDs loading amount. Furthermore, NCQDs content normalized rate of BPF degradation monotonically decreases with NCQDs content, which is ascribed to the gradual agglomeration of NCQDs on surface of Al<sub>2</sub>O<sub>3</sub>. Based on the degradation intermediates identified by GC-MS, two main degradation pathways are proposed for the degradation of BPF on the catalyst. The present findings highlight supported NCQDs as an effective catalyst for the catalytic activation of PDS for the degradation of endocrine disrupting chemicals.

## Acknowledgements

The financial support from the National Natural Science Foundation of China (no. 21577056 and 21507056), and the Natural Science Foundation of Jiangsu Province (BK20150568) is gratefully acknowledged.

## Appendix A. Supplementary data

Supplementary material related to this article can be found, in the online version, at doi:<https://doi.org/10.1016/j.apcatb.2018.07.032>.

## References

- [1] K. Inoue, S. Murayama, K. Takeba, J. Food Compos. Anal. 16 (2002) 497–506.
- [2] C.Y. Liao, K. Kannan, Arch. Environ. Con. Tox. 67 (2014) 50–59.
- [3] C.Y. Liao, F. Liu, Y. Guo, H.-B. Moon, H. Nakata, Q. Wu, K. Kannan, Environ. Sci. Technol. 46 (2012) 9138–9145.
- [4] S.J. Song, M.Y. Song, L.Z. Zeng, T. Wang, R.Z. Liu, T. Ruan, G.B. Jiang, Environ. Pollut. 186 (2014) 14–19.
- [5] Y.J. Yang, L.B. Lu, J. Zhang, Y. Yang, Y.N. Wu, B. Shao, J. Chromatogr. A 1328 (2014) 26–34.
- [6] K. Yamasaki, S. Noda, N. Imatanaka, Y. Yakabe, Toxicol. Lett. 146 (2004) 111–120.
- [7] N. Higashihara, K. Shiraiishi, K. Miyata, Y. Oshima, Y. Minobe, K. Yamasaki, Arch. Toxicol. 81 (2007) 825–832.
- [8] S. Kitamura, S. Sanoh, R. Kohta, T. Suzuki, K. Sugihara, N. Fujimoto, S. Ohta, J. Health Sci. 49 (2003) 298–310.
- [9] K. Satoh, K. Ohayama, N. Aoki, M. Iida, F. Nagai, Food Chem. Toxicol. 42 (2004) 983–993.
- [10] T. Stroheker, K. Picard, J.C. Lhuillier, M.C. Canivenc-Lavier, M.C. Chagnon, Food Chem. Toxicol. 42 (2004) 887–897.
- [11] Z.J. Liu, K.D. Lin, J. Gan, Environ. Pollut. 159 (2011) 2546–2551.
- [12] J.Q. Liu, X.R. Zhang, Water Res. 65 (2014) 64–72.
- [13] J.Q. Liu, X.R. Zhang, Y. Li, Environ. Sci. Technol. 51 (2017) 58–67.
- [14] M.T. Yang, X.R. Zhang, Environ. Sci. Technol. 47 (2013) 10868–10876.
- [15] L. Zhang, F. Pan, X.Y. Liu, L.J. Yang, X.Q. Jiang, J.C. Yang, W. Shi, Chem. Eng. J. 218 (2013) 238–246.
- [16] R. Tanwar, S. Kumar, U.K. Mandal, J. Photoch. Photobiol. A 333 (2017) 105–116.
- [17] H. Cabana, J.P. Jones, S.N. Agathos, Eng. Life Sci. 7 (2007) 429–456.
- [18] S.B. Hammouda, F.P. Zhao, Z. Safaei, D.L. Ramasamy, B. Doshi, M. Sillanpää, Appl. Catal. B Environ. 233 (2018) 99–111.
- [19] C.M. Park, J.Y. Heo, D.J. Wang, C.M. Su, Y.M. Yoon, Appl. Catal. B Environ. 225 (2018) 91–99.
- [20] A.D. Bokare, W. Choi, J. Hazard. Mater. 275 (2014) 121–135.
- [21] J.E. Silveira, W.S. Paz, P. Garcia-Munoz, J.A. Zazo, J.A. Casas, Appl. Catal. B Environ. 249 (2017) 314–321.
- [22] J.M. Monteagudo, A. Durán, R. González, A.J. Expósito, Appl. Catal. B Environ. 176–177 (2015) 120–129.
- [23] C.D. Qi, X.T. Liu, C.Y. Lin, H.J. Zhang, X.W. Li, J. Ma, Chem. Eng. J. 315 (2017) 201–209.
- [24] S.N. Su, W.L. Guo, C.L. Yi, Y.Q. Leng, Z.M. Ma, Ultrason. Sonochem. 19 (2012) 469–474.
- [25] H. Lin, X. Zhong, C. Ciotonea, X.H. Fan, X.Y. Mao, Y.T. Li, B. Deng, H. Zhang, S. Royer, Appl. Catal. B Environ. 230 (2018) 1–10.
- [26] S. Indrawirawan, H.Q. Sun, X.G. Duan, S.B. Wang, Appl. Catal. B Environ. 179 (2015) 352–362.
- [27] P.H. Shi, R.J. Su, F.Z. Wan, M.C. Zhu, D.X. Li, S.H. Xu, Appl. Catal. B Environ. 123–124 (2012) 265–272.
- [28] D.G. Li, X.G. Duan, H.Q. Sun, J. Kang, H.Y. Zhang, M.O. Tade, S.B. Wang, Carbon 115 (2017) 649–658.
- [29] H.Q. Sun, C.K. Kwan, A. Suvorova, H.M. Ang, M.O. Tadé, S.B. Wang, Appl. Catal. B Environ. 154–155 (2014) 134–141.
- [30] X.G. Duan, C. Su, L. Zhou, H.Q. Sun, A. Suvorova, T. Odedairo, Z.H. Zhu, Z.P. Shao, S.B. Wang, Appl. Catal. B Environ. 194 (2016) 7–15.
- [31] X.G. Duan, Z.M. Ao, H.Q. Sun, L. Zhou, G.X. Wang, S.B. Wang, Chem. Commun. 51 (2015) 15249–15252.
- [32] X.G. Duan, H.Q. Sun, Y.X. Wang, J. Kang, S.B. Wang, ACS Catal. 5 (2015) 553–559.
- [33] H.Q. Sun, S.Z. Liu, G.L. Zhou, H.M. Ang, M.O. Tadé, S.B. Wang, ACS Appl. Mater. Interfaces 4 (2012) 5466–5471.
- [34] H. Chen, K.C. Carroll, Environ. Pollut. 215 (2016) 96–102.
- [35] S.Y. Yang, T. Xiao, J. Zhang, Y.Y. Chen, L. Li, Sep. Purif. Technol. 143 (2015) 19–26.
- [36] X. Cheng, H.G. Guo, Y.L. Zhang, X. Wu, Y. Liu, Water Res. 73 (2015) 304–310.
- [37] L. Tang, Y.N. Liu, J.J. Wang, G.M. Zeng, Y.C. Deng, H.R. Dong, H.P. Feng, J.J. Wang, B. Peng, Appl. Catal. B Environ. 231 (2018) 1–10.
- [38] Y.-C. Lee, S.-L. Lo, J. Kuo, C.-P. Huang, J. Hazard. Mater. 261 (2013) 463–469.
- [39] H. Lee, H.-J. Lee, J. Jeong, J. Lee, N.-B. Park, C. Lee, Chem. Eng. J. 266 (2015) 28–33.
- [40] H.Q. Sun, C.K. Kwan, A. Suvorova, H.M. Ang, M.O. Tadé, S.B. Wang, Appl. Catal. B Environ. 154–155 (2014) 134–141.
- [41] B.J. Moon, Y. Oh, D.H. Shin, S.J. Kim, S.H. Lee, T.-W. Kim, M. Park, S. Bae, Chem.

- Mater. 28 (2016) 1481–1488.
- [42] F.B. Su, X.S. Zhao, L. Lv, Z.C. Zhou, Carbon 42 (2004) 2821–2831.
- [43] E. Aneggi, C. de Leitenburg, J. Llorca, A. Trovarelli, Catal. Today 197 (2012) 119–126.
- [44] Y. Otake, R.G. Jenkins, Carbon 31 (1993) 109–121.
- [45] Y.X. Wang, Y.B. Xie, H.Q. Sun, J.D. Xiao, H.B. Cao, S.B. Wang, ACS Appl. Mater. Interfaces 8 (2016) 9710–9720.
- [46] R. Arrigo, M. Havecker, R. Schlogl, D.S. Su, Chem. Commun. (2008) 4891–4893.
- [47] J.F. Hou, S.S. Yang, H.Q. Wan, H.Y. Fu, X.L. Qu, Z.Y. Xu, S.R. Zheng, Chemosphere 167 (2018) 485–493.
- [48] T. Zhang, D.Q. Huang, Y. Yang, F.Y. Kang, J.L. Gu, Polymer 53 (2012) 6000–6007.
- [49] M. Bayat, H. Yang, F. Ko, Polymer 52 (2011) 1645–1653.
- [50] P. Li, T.-J. Zhao, J.-H. Zhou, Z.-J. Sui, Y.-C. Dai, W.-K. Yuan, Carbon 43 (2005) 2701–2710.
- [51] S. Zhang, H.H. Song, P. Guo, J.S. Zhou, X.H. Chen, Carbon 48 (2010) 4211–4214.
- [52] X.F. Sun, Y.L. Xu, P. Ding, G.G. Chen, X.Y. Zheng, R. Zhang, L. Li, J. Power Sources 255 (2014) 163–169.
- [53] P. Zhang, F. Jiang, H. Chen, Chem. Eng. J. 234 (2013) 195–202.
- [54] N. Jaafarzadeh, F. Ghanbari, M. Ahmadi, Chemosphere 169 (2017) 568–576.
- [55] M. Muruganandham, M. Swaminathan, Sol. Energy Mater. Sol. C 81 (2004) 439–457.
- [56] H. Chen, Z.Y. Xu, H.Q. Wan, J.J. Zheng, D.Q. Yin, S.R. Zheng, Appl. Catal. B: Environ. 96 (2010) 307–313.
- [57] X.G. Duan, H.Q. Sun, J. Kang, Y.X. Wang, S. Indrawirawan, S.B. Wang, ACS Catal. 5 (2015) 4629–4636.
- [58] J. Zhou, K. Wu, W.J. Wang, Y.X. Han, Z.Y. Xu, H.Q. Wan, S.R. Zheng, Appl. Catal. B Environ. 162 (2015) 85–92.
- [59] D. Ouyang, J.C. Yan, L.B. Qin, Y. Chen, L. Han, A.Q. Su, W.Y. Zhang, H. Ni, M.F. Chen, Chemosphere 184 (2017) 609–617.
- [60] W.-D. Oh, G. Lisak, R.D. Webster, Y.-N. Liang, A. Veksha, A. Giannis, J.G.S. Moo, J.-W. Lim, T.-T. Lim, Appl. Catal. B Environ. 233 (2018) 120–129.
- [61] G.D. Fang, J. Gao, D.D. Dionysiou, C. Liu, D.M. Zhou, Environ. Sci. Technol. 47 (2013) 4605–4611.
- [62] P. Neta, R.E. Huie, A.B. Ross, J. Phys. Chem. Ref. Data 17 (1988) 1027–1038.
- [63] C.D. Qi, X.T. Liu, J. Ma, C.Y. Lin, X.W. Li, H.J. Zhang, Chemosphere 151 (2016) 280–288.
- [64] X. Qin, S.W. Fang, L. Zhao, P.H. Shi, J.C. Fan, Y.L. Min, Q.J. Xu, W.F. Yao, Sci. Total Environ. 601–602 (2017) 99–108.
- [65] S.H. Bossmann, E. Oliveros, S. Göb, S. Siegwart, E.P. Dahmen, L. Payawan, M. Straub, M. Wörner, A.M. Braun, J. Phys. Chem. A 102 (1998) 5542–5550.
- [66] V. Salomatova, I. Pozdnyakov, P. Sherin, V. Grivin, V. Plyusnin, J. Photochem. Photobio. A 305 (2015) 45–50.
- [67] H. Lu, Z.H. Weng, H. Wei, J.T. Zhou, J. Wang, G.F. Liu, W.Q. Guo, J. Chem. Technol. Biotechnol. 92 (2017) 854–860.
- [68] M. Suzuki, T. Sugiyama, E. Musashi, Y. Kobiyama, A. Kashiwada, K. Matsuda, K. Yamada, J. Appl. Polym. Sci. 118 (2010) 721–732.
- [69] O. Ballesteros, A. Zafra, A. Navalón, J.L. Vilchez, J. Chromatogr. A 1121 (2006) 154–162.
- [70] R. Thirivenkatachari, T.O. Kwon, I.S. Moon, Sep. Sci. Technol. 40 (2005) 2871–2888.
- [71] Z.B. Guo, R. Feng, J. Hazard. Mater. 163 (2009) 855–860.